RESEARCH

Antibacterial Effect of Copper Oxide Nanoparticles Prepared by Laser Production in Water Against *Staphylococcus aureus* and *Escherichia coli*

Sara Fadhil Abbas[1] · Adawiya J. Haider[2] · Sharafaldin Al-Musawi[3] · Murtadha Kadhim Selman[4]

Abstract

The rates of mortality and morbidity from treatment failures have increased due to microorganisms' growing resistance to antimicrobial medicines, signaling a severe hazard in the near future. Copper oxide (CuO) nanoparticles (NPs) were prepared using the laser penetration in water (LPW) method, which is regarded as an innovative and effective technique for producing a wide range of nanomaterials. The physical properties of the prepared NPs were studied by identifying them by dynamic light scattering (DLS), UV–visible spectroscopy (UV–Vis), Fourier transform infrared spectroscopy (FTIR), X-ray diffraction (XRD), field emission scanning electron microscope (FESEM), and energy-dispersive X-ray analysis (EDX). The absorption spectrum showed two peaks, one with a modest intensity at 650 nm and the other at 280 nm. In the optical characteristics study, the band gaps estimated for the CuO NPs are 3.6 eV. XRD shows the prepared CuO NPs have a polycrystalline structure with a pre-indication particle size of approximately 35 nm. The DLS results showed that the synthesized CuO nanoparticle has 35.19 ± 12.82 nm in size and -21.3 ± 6.56 in charge. FESEM image shows that CuO NPs have a homogeneous distributed spherical shape with some accumulation NPs in a cauliflower-like shape. Antibacterial activity of the prepared nanoparticles was tested against two types of bacterial strains, gram-positive bacteria *Staphylococcus aureus* (*S. aureus*) and gram-negative bacteria *Escherichia coli* (*E. coli*), isolated from the infected wounds. $AgNO_3$ was used as a control to compare with different concentrations of CuO NPs. The result indicated the antibacterial activity of CuO NPs was concentration-dependent and exceeded the antibacterial activity of the control agent ($AgNO_3$). At CuO NPs, the maximum concentration used was 200 μg/ml, and the inhibition zone was 16.5 mm and 15 mm for *E. coli* and *S. aureus*, respectively.

Keywords Copper oxide · Laser · Antibacterial · *Staphylococcus aureus* · *Escherichia coli*

Introduction

Infectious diseases induced by bacteria affect millions of people worldwide [1, 2]. Although many generations of antibiotics have been developed, the continuous rise in bacterial drug resistance is becoming an increasing concern for public health, driving the need for new antibacterial therapies [3, 4]. There are many reports in the literatures [5, 6] that show encouraging results about the activity of different drugs and antimicrobial formulations in the form of nanoparticles [7, 8]. Several promising antibacterial agents have emerged, including metal oxide nanoparticles, which means as the size of materials is reduced to the nanometer regime [9], the resulting physical, chemical, and biological properties change noticeably [10, 11].

Metal oxides represent the most diverse class of materials with properties covering almost all aspects of Materials Science and Physics. Nanoparticulate metal oxides are particularly interesting in that they can be prepared with extremely high surface areas and with unusual crystal morphologies that possess numerous edges/corners and other reactive surface sites [12]. These modified features allow the NPs to interact in a unique manner with cell biomolecules and thus facilitate the physical transfer of NPs into the inner cellular structures [13].

✉ Adawiya J. Haider
adawiyajhaider@gmail.com

1 Department of Laser and Optoelectronics Engineering, College of Engineering, Al-Nahrain University, Jadriya, Baghdad, Iraq

2 Applied Sciences Department/Laser Science and Technology Branch, University of Technology, Baghdad, Iraq

3 College of Food Sciences, Al-Qasim Green University, Babylon Province, Iraq

4 Ministry of Education, Babylon Education Directorate, Babylon Province, Iraq

Copper oxide nanoparticles (CuO NPs) have attracted a lot of interest among metal nanoparticles because of their nontoxicity, accessibility, availability in nature, simplicity of fabrication, and remarkable photovoltaic properties [14, 15]. CuO NPs have been used in a variety of applications, including field emission emitters, high-temperature superconductors, solar energy conversion, and sensing catalysis [16, 17]. CuO NPs have several properties including high antimicrobial activity, good thermal stability, and outstanding biocompatibility; hence, they can be used as an antibacterial agent [18, 19]. It can be easily mixed with polymers providing the composites with unique physio-chemical properties [20].

CuO NPs' precise antibacterial mode of action is still not fully known, although it is becoming clear that numerous processes are involved in the work. The antibacterial process of CuO NPs killing bacteria could be summarized by the production of reactive oxygen species (ROS); proteins and DNA are reacted with CuO NPs, destroying cell wall membranes [21]. By these techniques, CuO NPs can destroy many types of microorganisms. The supposed mechanism of CuO NPs killing the bacteria is summarized in Fig. 1. Actuality, CuO NPs' primary antibacterial action is not the Cu ions released by dissolution outside of the bacterial cell [22]. The latest study revealed that less than 50% of the total cytotoxicity brought on by CuO NPs was supplied by dissolved copper ions [23]. ROS-induced oxidative stress is essential for copper's antibacterial action. CuO NPs may produce ROS through a variety of methods in addition to immediately leaching ions, such as the alteration of mitochondrial membrane potential and the production of singlet oxygen, which both facilitate DNA deterioration [24].

Among several nano-/micro-fabrication techniques [25] used to produce copper oxide, the pulsed laser ablation (production) in water (LPW) is considered a promising tool with high efficiency to achieve the purpose of varying particle sizes of the prepared nanostructured materials [26, 27]. This technique could be represented as a simple [7], effective [28], and inexpensive tool to synthesize different desired materials with high purity [29]. Besides, the synthetic of nanostructured materials inside the liquid route prevents the formation of contamination that could be harmful to the surroundings as happened by other synthetic techniques [30, 31]. In addition, the preservation of the original materials' elemental stoichiometry is facilitated by laser production in water [32]. LPW has high flexibility in choosing ablation parameters and environments [33, 34]. These entire reasons make this technique one of the common techniques to be chosen for the production of desired characteristic nanoparticles.

The present study aimed to prepare CuO NPs using laser production in water; study the structural, morphological, and chemical composition, bond type, and optical physical properties to calculate the band gap; verify the purity of the CuO NPs; and define the mechanism of the antimicrobial activity against the most common pathogenic bacteria (*Staphylococcus aureus* and *Escherichia coli*).

Fig. 1 Antibacterial mechanism of CuO NPs
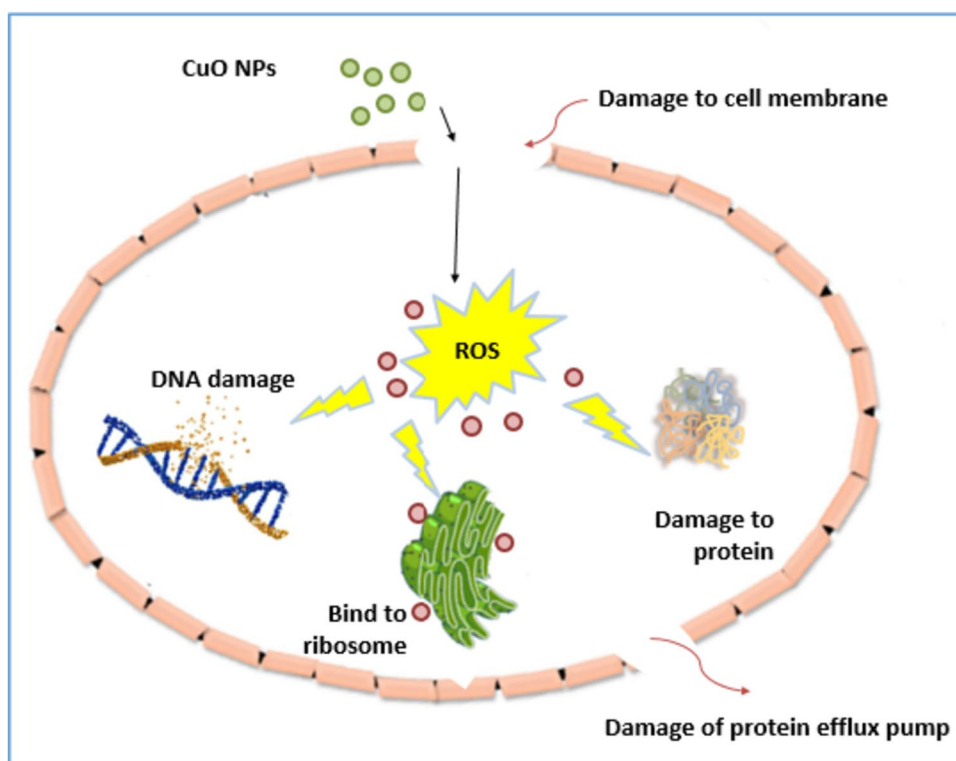
Experimental Work

Materials and Method

High-purity copper sheets (99.999%, BDH Chemical Ltd., Pool, England) were used to produce CuO NPs by laser production in water technique. A 10-cm focus lens was used to collimate the laser beam on the sample. The copper sheet dimension (10 cm × 10 cm × 0.1 cm) was cut into a small piece (1 cm × 1 cm). Figure 2a shows the copper sheet plate before cutting. To eliminate any leftover organic substances, the target was polished and washed with ethanol, acetone, and deionized water. The small pieces of target were impressed underlying 5 ml of deionized water (DW) in a glass vessel at room temperature. The procedure involved using a Q-switched Nd:YAG laser (Huafei Tongda Technology-DIAMOND-288 pattern EPLS) with wavelength 1064 nm, frequency 1 Hz, pulse width 10 ns, and 1000 mJ laser energy, and the exposure time was 25 min. Figure 2b shows the effect of the laser ablation and the production of CuO NPs by changing the DW color into green.

Mechanism of Generating Nanoparticles

To generate a given NP size distribution, yield, and shape, a number of variables (laser pulse width, laser fluence, repetition rate, kind of liquid media, etc.) must be adjusted [35].

Several physicochemical processes are involved in the generation of NPs during LPW. The first stage involves the laser's interaction with the liquid medium, which includes the creation of electron clouds because of photon absorption by the molecules of the liquid media. The laser will interact with each liquid medium differently, producing various results [36]. The interaction of the laser beam with distilled water produces $H^{\bullet}$ and OH^{-} ions. The second stage of LPW involves the laser's interaction with the copper target. In this phase, nuclei are formed, the plasma plume is formed, electron clouds are involved in the ablation process, cavitation bubbles are formed, and so on [37]. In stage 3 of LPW, nuclei develop into NPs inside the cavitation bubble, ions from the liquid medium are involved in the nucleation process, NPs grow, NPs collide, NPs aggregate, and NPs age. Figure 3 shows the steps of LPW mentioned above. It is challenging to include all of the physicochemical equations that regulate the LPW process in a single simulation [38].

Characterization Techniques

The physical characterization of copper oxide NPs was measured using different techniques. The crystal structure of the synthesized CuO NPs was measured by AERIS PANalytical XRD device with Cu-Kα radiation source at 2θ angle = 10–80°. The bond vibrations of NPs in the range of 400–4000 cm^{-1} were measured using 8000 Series FTIR. The optical absorption of colloidal nanoparticles was measured (200–800) via UV–Vis spectrophotometer with a double beam (Shimadzu UV-1800). The particle size and its distribution were measured by dynamic light scattering (DLS; Malvern Zetasizer ZS, Malvern, UK). The morphology of the nanostructures was examined with an Axia ChemiSEM FESEM and EDX.

Antibacterial Study

Two bacterial strains gram-positive *Staphylococcus aureus* (*S. aureus*) and gram-negative *Escherichia coli* (*E. coli*) were applied in this work. The agar plates for the antibacterial testing were incubated for 24 h to make sure there was no contamination. On separate agar plates, the isolated colonies of *S. aureus* and *E. coli* were put before being mixed with 100 ml of nutritional broth. At 37 °C and 100 rpm, the bacteria suspension was cultured in the shaker incubator for an entire night. For 48 h, the plates containing bacteria and CuO NPs were incubated at 37 °C. The synthesized CuO NPs were employed to test the antibacterial susceptibility at the following concentrations (25, 50, 100, 150, and 200 mg/ml). Each sample's inhibition zones were examined, and a meter ruler was used to measure each inhibition zone's diameter. The average result of this antimicrobial assay was noted [35].

Fig. 2 **a** Photograph of the copper sheet. **b** Photograph of the production of CuO NPs after the ablation process
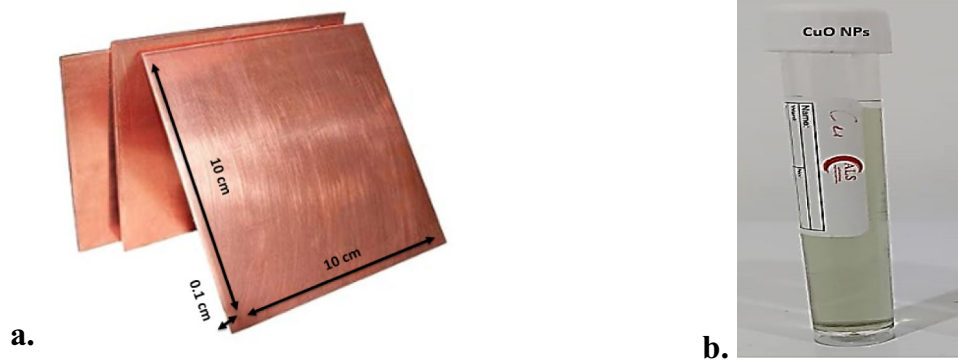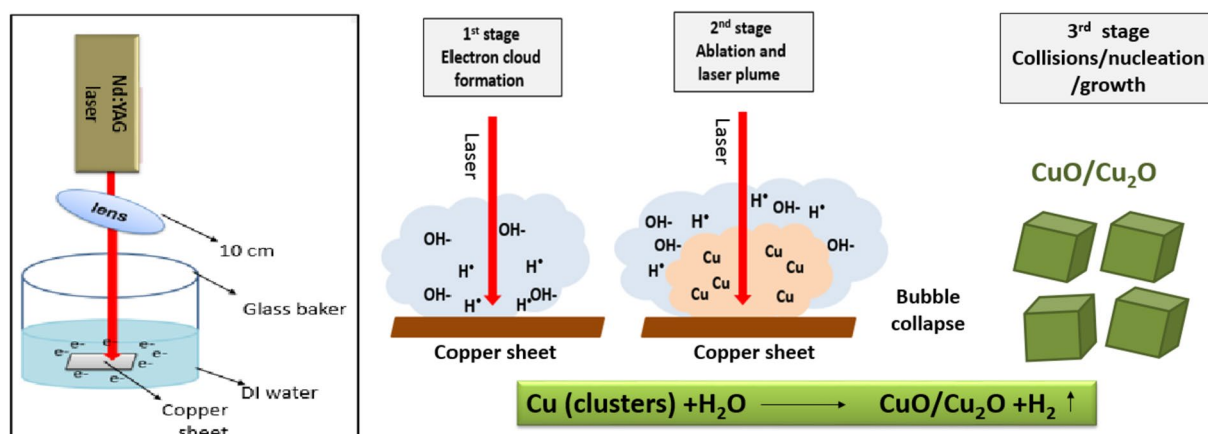
Fig. 3 Laser ablation in water (stages of CuO NP formation)

Statistical Analysis

The mean $\pm$ standard division (SD) was used for the statistical analysis of our results. Excel was also used to evaluate statistical significance. Results $p < 0.05$ and $p < 0.01$ are defined as the criteria for statistical significance.

Result and Discussion

The prepared colloidal CuO NPs were dropped on a glass slab (1 cm $\times$ 1 cm) by vaporizing the suspension. The XRD of the copper sheet and the CuO NPs recorded by using Cu-Kα radiation is shown in Fig. 4a and b, respectively.

Figure 4a shows the XRD pattern of the copper sheet used to produce CuO NPs. It can be clearly noticed that the presence of sharp peaks obtained at 2θ equal to 51°, 74.6°, and 90.3° represents the appearance of copper peak orientations (200), (220), and (311), respectively. This conflicts with the Cu card (JCPDS No. 040836). Figure 4b illustrates the XRD analysis of CuO NPs. The spike shape of the curve and the produced peaks appeared to be related to the use of a glass slab as a substrate for XRD analysis, making the background noisy. The XRD of the CuO NPs indicates peaks were 32.6°, 38.9°, and 46.25°, which correspond to (110), (111), and (−112) planes of CuO NPs. The crystalline size obtained for these peaks was 45.1 nm, 18.4 nm, and 38.7 nm, respectively. These results are in good agreement with
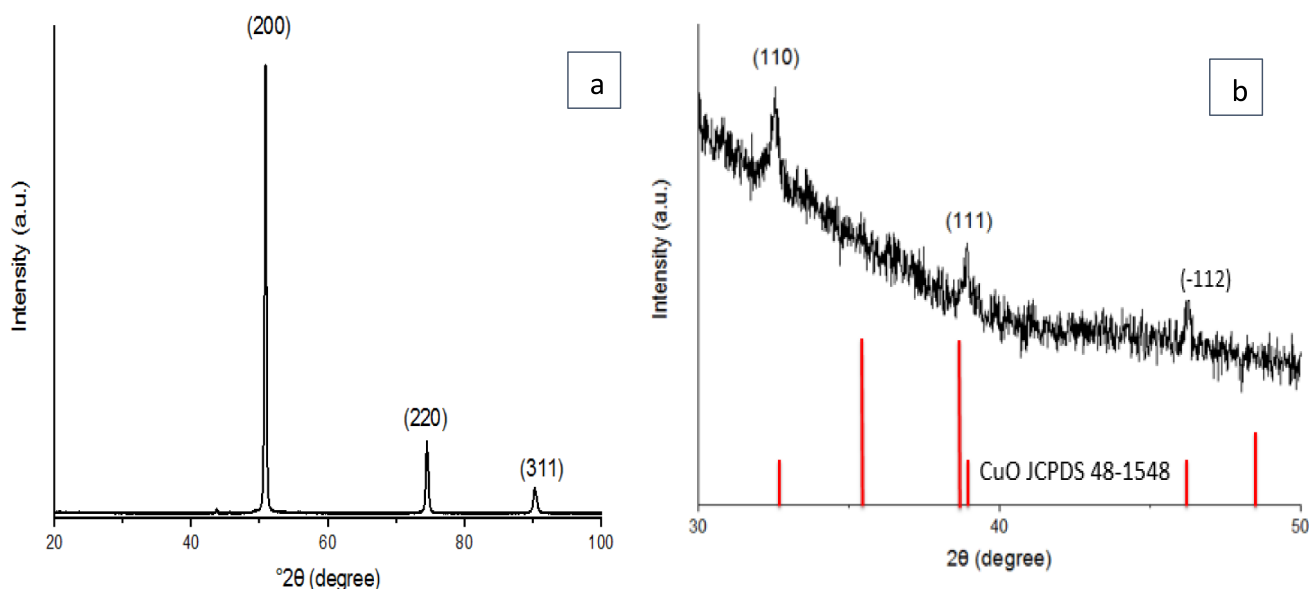

Fig. 4 XRD of **a** pure copper sheet and **b** CuO NPs deposited on glass substrate

Table 1 The XRD structural parameters of CuO NPs

Peak position	Orientation	Crystallite size	d-spacing (Å)
32.6	(110)	45.1 nm	2.74548
38.9	(111)	18.4 nm	2.31046
46.25	(−112)	38.7 nm	1.96102

the standard diffraction peak of CuO (JCPDS 48–1548). The peaks of the prepared CuO NPs tend to be broadly related to the size of the particles that make the diffraction, which means smaller particle size makes broader peaks. The peak position, size orientation, and d-spacing indicated are summarized in Table 1. The average particle size of the sample was estimated by using the Debye–Scherrer equation [39, 40]:

$$D = \frac{0.9\lambda}{\beta \cos\theta}. \tag{1}$$

λ is the wavelength (Cu-Kα), β is the full width at the half-maximum, and θ is the diffraction angle. The prepared sample has a polycrystalline structure with an average particle size of approximately 35 nm.

FTIR spectroscopy was performed to identify the functional groups of the synthesized copper oxide nanoparticles. The FTIR transmittance spectra of the suspended nanoparticles were obtained in the range from 4000 to 400 cm^{-1}. Figure 5 shows the FTIR spectrum of all prepared samples of CuO NPs. According to Fig. 5, it can be observed

that the maximum absorption is at 3430 cm^{-1}, 2356 cm^{-1}, 1633 cm^{-1}, and 678 cm^{-1}. A broad band at 3430 cm^{-1} appeared and was assigned to the O–H stretching mode of the hydroxyl group [41]. Metals generally give absorption bands in regions above [42]. The broad absorption peak at around 3430 cm^{-1} is caused by the adsorbed water molecules since the nanocrystalline materials exhibit a high surface to volume ratio and thus absorb moisture [43]. In addition, a band located at 1633 cm^{-1} is related to the deformation and elongation vibration of the O–H bond, indicating the presence of water molecules (H_2O). The peak at 2356 cm^{-1} was attributed to O=C=O stretching carbon dioxide contamination from the atmosphere. Previous studies mention the vibrational modes of Cu–O in CuO NPs are responsible for the high absorption peaks seen in the 500–700 cm^{-1} range [44, 45]. The observed transmitted band found at 678 cm^{-1} is attributed to the appearance of Cu–O [45, 46]. All the values are tabulated with their corresponding bonds in Table 2.

Figure 6 shows the UV–Vis spectra of the colloidal dispersion containing particles synthesized by laser ablation of the Cu target. The figure shows the presence of two regions of absorption (280 and 650 nm). The peak that appeared at 280 nm results from the inter-band transition of the copper electron from the deep level of the valence band, while the peak at 650 nm, commonly known as the surface plasmon resonance (SPR) peak, results from the inter-band transition of the copper electron from the upper level of the valence band. These results are close to the findings reported by Swarnkar et al. [47].

Fig. 5 The FTIR spectrum of CuO NPs
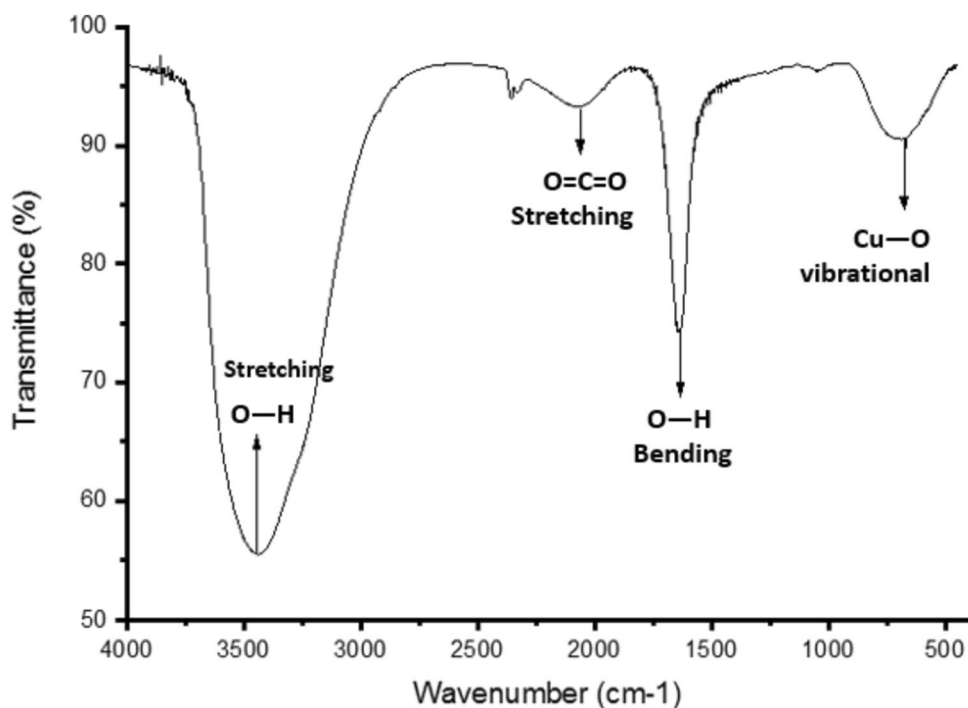
Table 2 The transmission bonds and functional groups of the synthesized CuO NPs

Wavenumber	Functional group
3430 cm^{-1}	O–H stretching vibration
2356 cm^{-1}	O=C=O stretching
1633 cm^{-1}	O–H bending vibration
678 cm^{-1}	Cu–O vibrational mode

The fundamental absorption, which corresponds to electron excitation from the valence band to the conduction band, can be used to determine the value of the optical band gap. The relationship between the absorption coefficients α and the incident photon energy hυ can be written as [48]:

$$(\alpha h\upsilon) = A\ (h\upsilon - E_g)^n, \tag{2}$$

where α is the absorption coefficient, hυ is the photon energy, A is the material-dependent constant, Eg is the band gap energy, and "n" is a constant associated with the direct transition in semiconductors. The absorption coefficient of the copper oxide was estimated using the following formula [49]:

$$\alpha = 2.303\frac{A}{d}, \tag{3}$$

where d and A are the path length and absorbance of the colloidal CuO NPs. To compute the direct band gap Eg for CuO NPs, we used extrapolating the linear region of the plot of $(\alpha h\upsilon)^2$ on (x-axis) vs. hυ on (y-axis) that was determined by the x-intercept. The direct band gap of CuO NPs is shown by

the intercept of the tangent to the plot on the *x*-axis. Figure 6 (inset) shows the band gap estimated using the Tauc method was 3.6 eV which coincides with the previous reports [50, 51]. The estimated band gap was larger than the previously reported value for bulk CuO (1.2 eV) [45]. This increased band gap is attributed to the lowered particle size. When the size of nanocrystals is smaller than the Bohr radius of the excited electron–hole pair, the quantum confinement effect occurs and the band gap energy starts to increase with the decrease in particle size [52].

DLS analysis was performed to learn more about the size and stability of the produced CuO NPs and the surface charge of NPs. In Fig. 7a, the average particle size distribution of CuO NPs was 35.19 ± 12.82 nm. From Fig. 7b, the stability of colloidal dispersion is confirmed by the optimal value achieved (− 21.3 ± 6.56 mV). This value is big enough to avoid the agglomeration of particles by electrostatic repulsion. The strong repelling force between the particles is indicated by the high absolute zeta potential value, which also inhibits aggregation [53]. The high negative surface charge of the particles serves as evidence that the homogeneity is caused by a repulsive force between them.

FESEM images of CuO NPs and particle size distribution are shown in Fig. 8a and b. The image shows a homogeneous distribution of nanoparticles in the form of spheres with approximately the same achieved size by the DLS test. By observing Fig. 8a, it can clearly see the accumulation of some spheres of NPs in a cauliflower-like shape. The nanoparticle diameter was calculated using the ImageJ program shown in Fig. 8b.

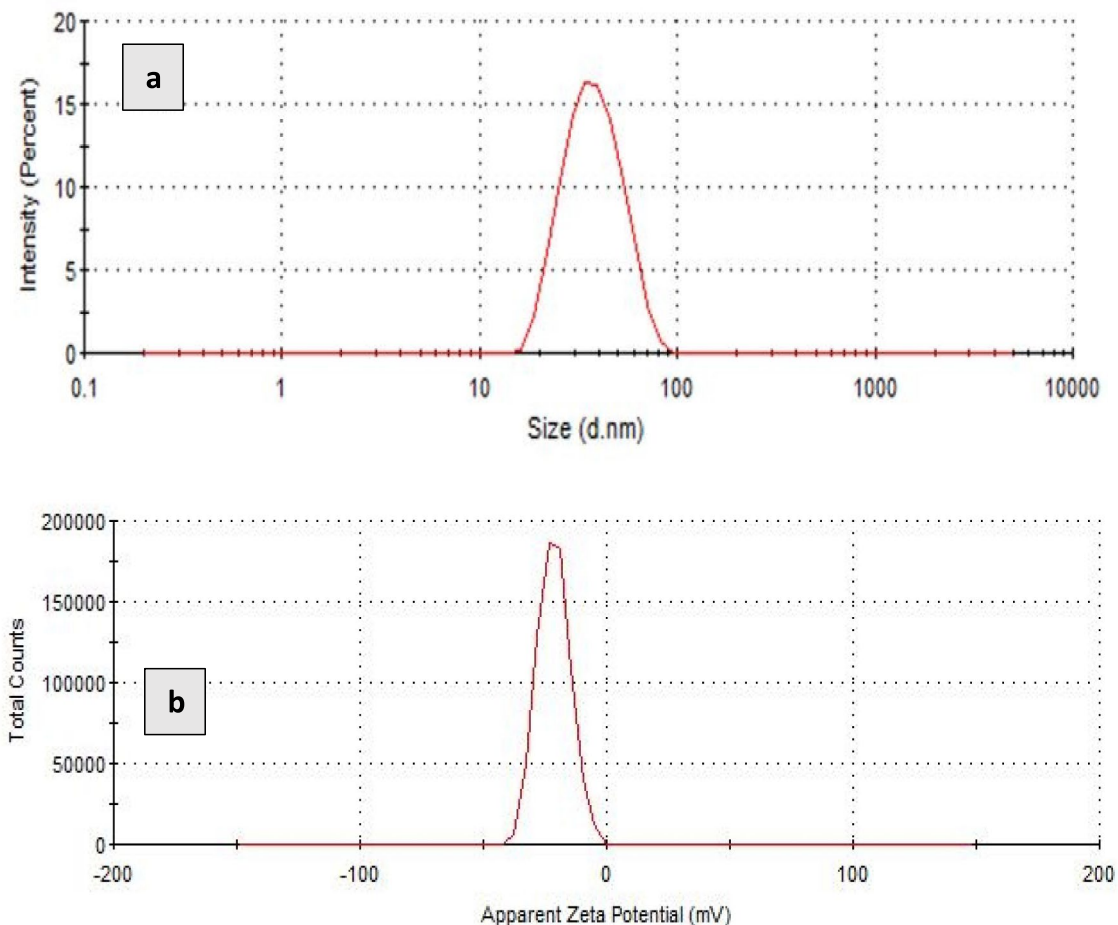**Fig. 6** UV–visible spectra of the collided CuO NPs (inset: band gap of CuO NPs)
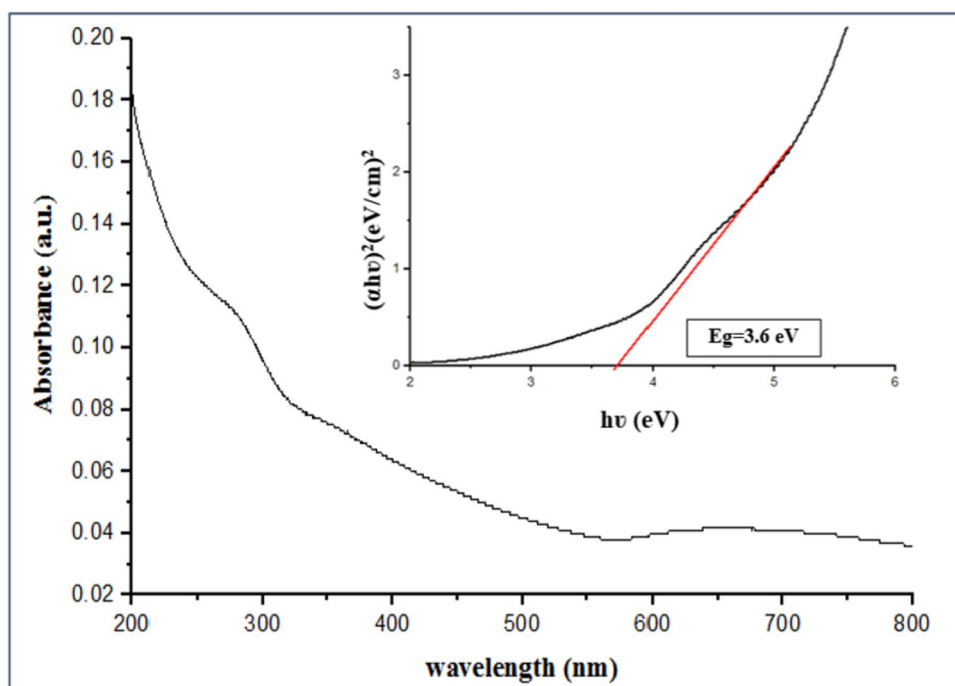
Fig. 7 DLS measurement: **a** particle size distribution, **b** zeta potential measurement

The corresponding energy-dispersive X-ray EDX results are presented in Fig. 9. The EDX spectra provide analytical data about the samples in both qualitative and quantitative forms. EDX data represent the appearance of a high percentage of Cu and O. The appearance of the carbon peak is due to the drop-casting of CuO NP suspension while it is
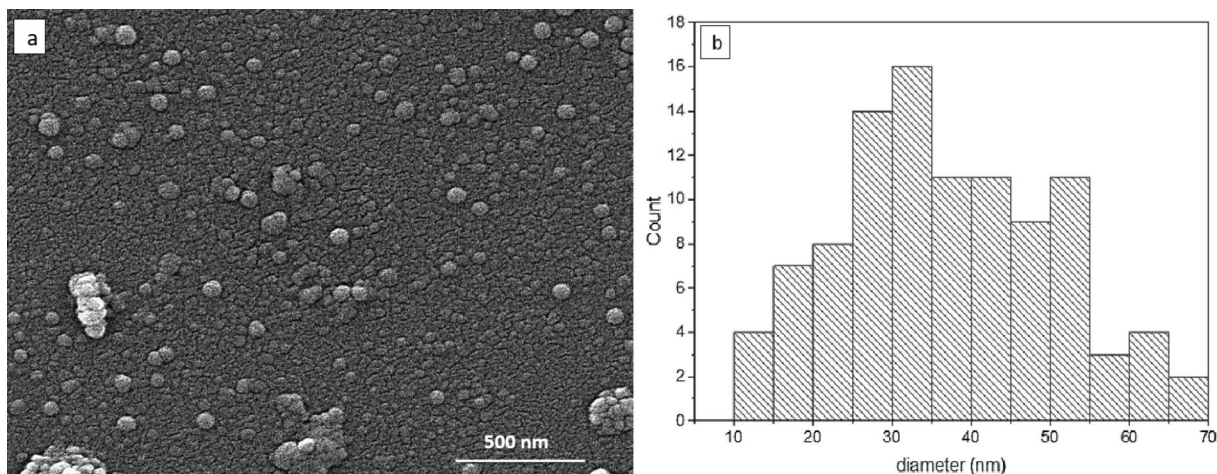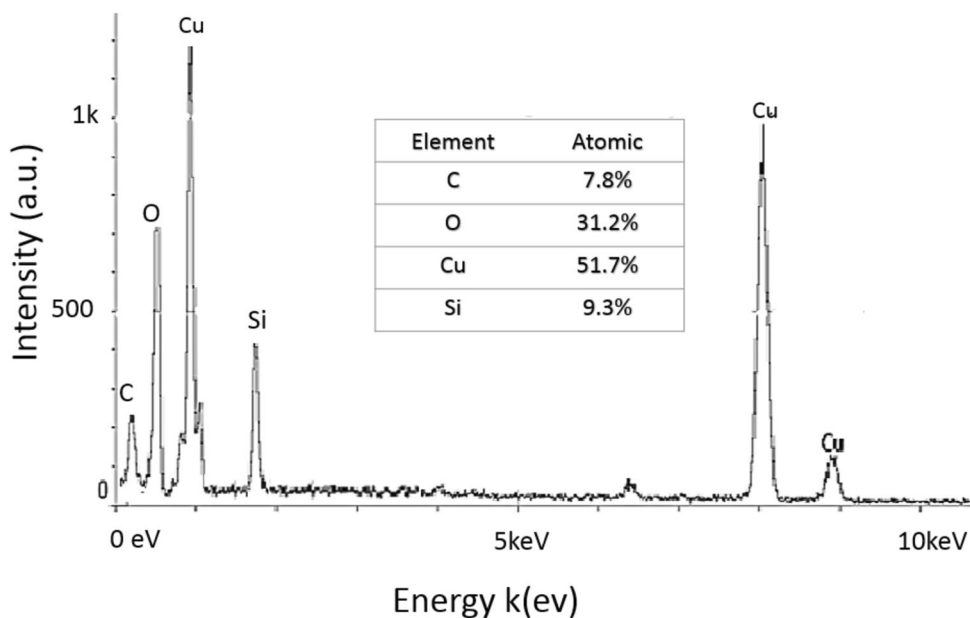

Fig. 8 **a** FESEM image of CuO NPs, **b** diameter distribution

Fig. 9 EDX results (table inset, the atomic percentage of elements)

| Element	Atomic
C	7.8%
O	31.2%
Cu	51.7%
Si	9.3%

exposed to carbon existing in the atmosphere. The presence of a silicon (Si) peak is a result of CuO NPs being deposited on a glass substrate for conducting an EDX analysis. The atomic percentage elements of the CuO NPs are presented in the table inset of Fig. 9.

Antibacterial Activity

Antibacterial activity is the killing or reduction of bacteria without overall toxicity to the body's tissue surrounding them [54]. The synthesized CuO nanoparticles' antibacterial

Fig. 10 Antibacterial activity of CuO NPs against *E. coli* and *S. aureus*. Data are presented as (mean $\pm$ SD (*$p < 0.05$; **$p < 0.01$; ***$p < 0.001$); $n = 3$)
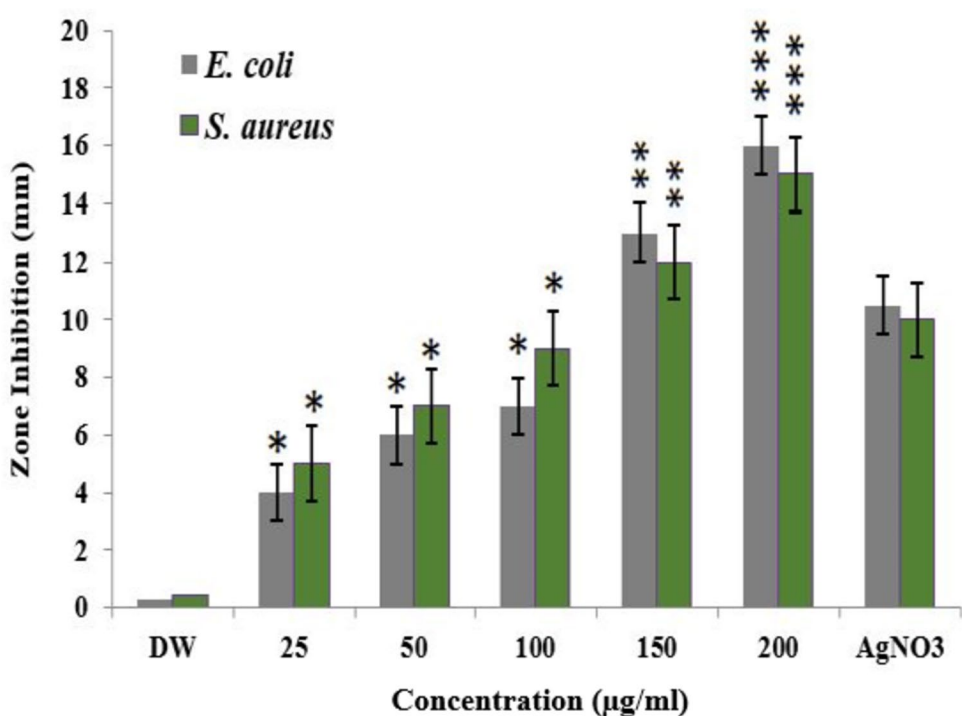
Fig. 11 Plate inhibition zone assay showing the antibacterial activity of **a** *E. coli* and **b** *S. aureus* (numbers 1, 2, and 3 refer to the concentrations 100, 150, and 200 µg/ml, respectively)
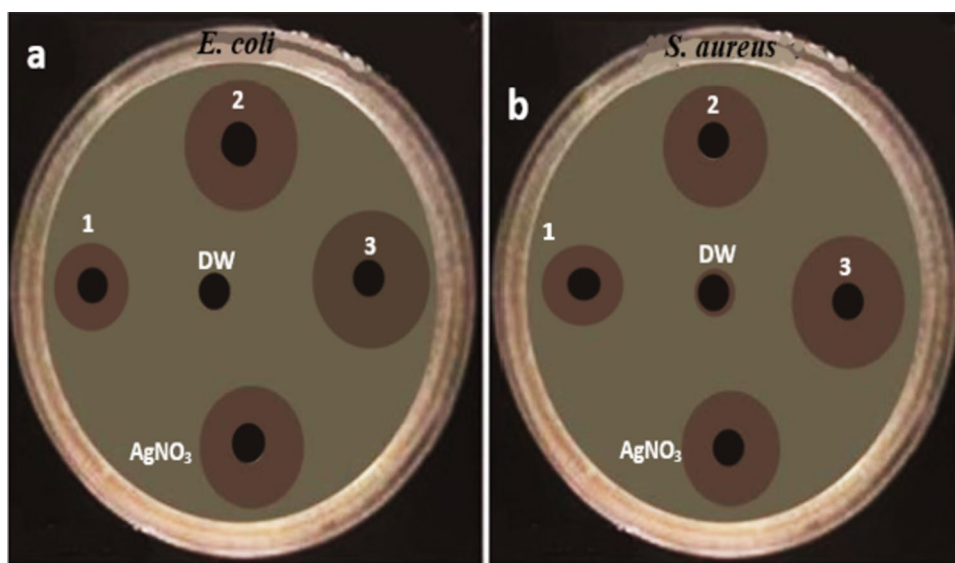
activity was evaluated using the agar well diffusion method. Figure 10 shows the inhibitory zone of CuO NPs against *E. coli* and *S. aureus*. The use of silver nitrate (AgNO$_3$) was as a calibrated agent and compared with different concentrations of CuO NPs. The synthesized CuO NPs were employed to test antibacterial susceptibility at the following concentrations: 25, 50, 100, 150, and 200 µg/ml. The inhibitory zone of CuO NPs was measured after 48 h of incubation. Particularly, it was discovered that the diameter of the inhibitory zone correlated with the number of nanoparticles present in the medium.

In comparison to the effect on gram-negative bacteria, the effect of CuO NPs on gram-positive bacteria growth was shown to be stronger at higher concentrations (150, 200 µg/ml) than gram-negative. This might be related to the alteration in the cell wall construction of these two classes [55]. CuO NPs have more antibacterial effects on gram-positive bacteria than gram-negative bacteria. Gram-positive bacteria have higher amounts of peptidoglycan and protein content in the cell wall. This behavior is due to copper having a higher affinity for proteins compared to lipids [21]. With respect to gram-positive *S. aureus*, it was found that the inhibitory zone sizes were ranging from 6 and 15 mm, as the nanoparticle concentration increased from 25 to 200 µg/ml. The inhibitory zones for gram-negative *E. coli* were found to have widths of 4 and 16.5 mm and nanoparticle concentrations of 25 and 200 µg/ml, respectively. The concentrations of 150 and 200 µg/ml exceeded the antibacterial activity of the control agent (AgNO$_3$). Figure 11 represents the inhibition zones of the maximum concentrations (100, 150, 200 µg/ml). It can clearly see the increase in the diameter of the inhibition zones as the concentration increased from 100 to 200 µg/ml. The lowest concentration of an antimicrobial that will prevent a microbe from growing visibly after an overnight incubation period, known as a minimum inhibitory concentration

(MIC), was 25 µg/ml for both strains. CuO NPs prepared using pulsed laser production in DW show a significant antibacterial action on both *E. coli* and *S. aureus*.

Conclusion

According to this study, the copper sheet was successfully ablated with an Nd:YAG laser after being submerged in distilled water to create copper oxide nanoparticles. Based on the findings of the current study, higher energy regions (1000 mJ) are used to produce the required concentration of CuO NPs with average particle sizes of approximately 35 nm in size, which is the most desired size. FTIR and the optical study show the appearance of copper oxide with a band gap equal to 3.6 eV for CuO NPs. XRD analysis shows the CuO nanoparticles are in polycrystalline structures. FESEM results show an aspherical structure with sometimes accumulation of some spheres of NPs in a cauliflower-like shape. Although the low concentration of CuO NPs was used in the antibacterial study, a significant antibacterial activity was observed from CuO nanoparticles synthesized because of the large surface area of NPs. The results demonstrated that copper oxide NPs produced by the LPW method might be used to eliminate dangerous and harmful bacteria because they possess antibacterial activity.

Declarations

Competing Interests The authors declare no competing interests.

References

1. Govindasamy GA, Mydin RBS, Harun NH, Sreekantan S (2021) Bactericidal potential of dual-ionic honeycomb-like ZnO-CuO nanocomposites from Calotropis gigantea against prominent pathogen associated with skin and surgical wound infections: Staphylococcus aureus. J Mater Sci Energy Technol 4:383–390

2. Govindasamy GA, Mydin RBS, Sreekantan S, Harun NH (2021) Compositions and antimicrobial properties of binary ZnO–CuO nanocomposites encapsulated calcium and carbon from Calotropis gigantea targeted for skin pathogens. J Sci Rep 11(1):99

3. Inam M et al (2019) Size and shape affects the antimicrobial activity of quaternized nanoparticles. J Polym Sci Part A Polym Chem 57(3):255–259

4. Govindasamy GA, Mydin RBSMN, Harun NH, Effendy WNFWE, Sreekantan S (2023) Giant milkweed plant-based copper oxide nanoparticles for wound dressing application: physicochemical, bactericidal and cytocompatibility profiles. J Chem Pap 77(2):1181–1200

5. Fresta M, Puglisi G, Giammona G, Cavallaro G, Micali N, Furneri PM (1995) Pefloxacine mesilate-and ofloxacin-loaded polyethylcyanoacrylate nanoparticles: characterization of the colloidal drug carrier formulation. J Pharm Sci 84(7):895–902

6. Couvreur P, Fattal E, Alphandary H, Puisieux F, Andremont A (1992) Intracellular targeting of antibiotics by means of biodegradable nanoparticles. J Control Release 19(1–3):259–267

7. Haider AJ, Thamir AD, Ahmed DS, Mohammad M (2016) Deposition of silver nanoparticles on multiwalled carbon nanotubes by chemical reduction process and their antimicrobial effects. In AIP Conf Proc 1758(1): AIP Publishing

8. Salman JAS, Kadhim AA, Haider AJ (2018) Biosynthesis, characterization and antibacterial effect of ZnO nanoparticles synthesized by Lactobacillus Spp. J Global Pharma Technol 10(03):348–355

9. Al-Kinani MA, Haider AJ, Al-Musawi S (2020) High uniformity distribution of Fe@ Au preparation by a micro-emulsion method. In IOP Conf Ser Mater Sci Eng 987(1):012013: IOP Publishing

10. Liu H et al (2007) Role of point defects in room-temperature ferromagnetism of Cr-doped ZnO. Appl Phys Lett 91(7):072511

11. Haider AJ, Alawsi T, Haider MJ, Taha BA, Marhoon HA (2022) A comprehensive review on pulsed laser deposition technique to effective nanostructure production: trends and challenges. Opt Quant Electron 8(54):488

12. Klabunde KJ et al (1996) Nanocrystals as stoichiometric reagents with unique surface chemistry. J Phys Chem 100(30):12142–12153

13. Rasmussen JW, Martinez E, Louka P, Wingett DG (2010) Zinc oxide nanoparticles for selective destruction of tumor cells and potential for drug delivery applications. Expert Opin Drug Deliv 7(9):1063–1077

14. Abbas RH, Kadhim A, Haleem AM (2022) The antibacterial activities of copper oxide nanoparticles synthesized using laser ablation in different surfactants against *Streptococcus mutans*. J Renew Mater

15. Govindasamy GA, Mydin RBS, Effendy WNFWE, Sreekantan S (2022) Novel dual-ionic ZnO/CuO embedded in porous chitosan biopolymer for wound dressing application: physicochemical, bactericidal, cytocompatibility and wound healing profiles. Mater Today Commun 33:104545

16. Chang Y-N, Zhang M, Xia L, Zhang J, Xing G (2012) The toxic effects and mechanisms of CuO and ZnO nanoparticles. Materials 5(12):2850–2871

17. Sawaby A, Selim M, Marzouk S, Mostafa M, Hosny A (2010) Structure, optical and electrochromic properties of NiO thin films. Phys B Condens Mater 405(16):3412–3420

18. Haider A, Al-Anbari R, Kadhim G, Jameel Z (2018) Synthesis and photocatalytic activity for TiO2 nanoparticles as air purification. MATEC Web Conf 162:05006

19. Mahdi SA et al (2021) Gene expression and apoptosis response in hepatocellular carcinoma cells induced by biocompatible polymer/magnetic nanoparticles containing 5-fluorouracil. Electron J Biotechnol 52:21–29

20. Amiri M, Etemadifar Z, Daneshkazemi A, Nateghi M (2017) Antimicrobial effect of copper oxide nanoparticles on some oral bacteria and candida species. J Dent Biomater 4(1):347

21. Ma X, Zhou S, Xu X, Du Q (2022) Copper-containing nanoparticles: mechanism of antimicrobial effect and application in dentistry-a narrative review. Front Surg 9:905892

22. Sabella S et al (2014) A general mechanism for intracellular toxicity of metal-containing nanoparticles. R Soc Chem 6(12):7052–7061

23. Wang Z, Li N, Zhao J, White JC, Qu P, Xing B (2012) CuO nanoparticle interaction with human epithelial cells: cellular uptake, location, export, and genotoxicity. Chem Res Toxicol 25(7):1512–1521

24. Hsiao I-L, Hsieh Y-K, Wang C-F, Chen I-C, Huang Y-J (2015) Trojan-horse mechanism in the cellular uptake of silver nanoparticles verified by direct intra-and extracellular silver speciation analysis. Environ Sci Technol 49(6):3813–3821

25. Dakhil GY, Salih RM, Hameed AM (2023) Influence of infill pattern, infill ratio on compressive strength and hardness of 3D printed polylactic acid (PLA) based polymer. J Appl Sci Nanotechnol 3(1)

26. Mostafa AM, Yousef SA, Eisa WH, Ewaida MA, Al-Ashkar EA (2017) Synthesis of cadmium oxide nanoparticles by pulsed laser ablation in liquid environment. Optik 144:679–684

27. Khashan KS, Abbas SF (2016) Characterization of InN nanoparticles prepared by laser as photodetector. Int J Mod Phys B 30(14):1650080

28. Yousif AA, Habubi NF, Haidar A (2012) Nanostructure zinc oxide with cobalt dopant by PLD for gas sensor applications. J Nano-Electron Phys

29. Kanitz A et al (2019) Review on experimental and theoretical investigations of the early stage, femtoseconds to microseconds processes during laser ablation in liquid-phase for the synthesis of colloidal nanoparticles. Plasma Sources Sci Technol 28(10):103001

30. McCarthy É et al (2022) Silver nanocolloid generation using dynamic Laser Ablation Synthesis in Solution system and dropcasting. Nano-Struct Nano-Objects 29:100841

31. Haider AJ, Sultan FI, Haider MJ, Hadi NM (2019) Spectroscopic and structural properties of zinc oxide nanosphere as random laser medium. Appl Phys A 125(4):260

32. Haider AJ, Al-Kinani MA, Al-Musawi S (2021) Preparation and characterization of gold coated super paramagnetic iron nanoparticle using pulsed laser ablation in liquid method. Key Eng Mater 886:77–85

33. Balachandran A, Sreenilayam SP, Madanan K, Thomas S, Brabazon D (2022) Nanoparticle production via laser ablation synthesis in solution method and printed electronic application-A brief review. Results Eng 100646

34. Al-Obaidy R, Hadier AJ, Al-Musawi S, Arsad N (2023) Study of the effects of solution types on concentration of iron oxide by Pulsed Laser Ablation in Liquid. J Appl Sci Nanotechnol 3(1):137–150

35. Albukhaty S, Al-Bayati L, Al-Karagoly H, Al-Musawi S (2022) Preparation and characterization of titanium dioxide nanoparticles and in vitro investigation of their cytotoxicity and antibacterial activity against Staphylococcus aureus and Escherichia coli. Anim Biotechnol 33(5):864–870

36. Amans D, Cai W, Barcikowski S (2019) Status and demand of research to bring laser generation of nanoparticles in liquids to maturity. Appl Surf Sci 488:445–454

37. Nyabadza A, Vázquez M, Coyle S, Fitzpatrick B, Brabazon D (2021) Magnesium nanoparticle synthesis from powders via pulsed laser ablation in liquid for nanocolloid production. Appl Sci 11(22):10974

38. Mostafa AM, Mwafy EA (2020) Synthesis of ZnO and Au@ ZnO core/shell nano-catalysts by pulsed laser ablation in different liquid media. J Mater Res Technol 9(3):3241–3248

39. Selvam NCS, Kumar RT, Kennedy LJ, Vijaya JJ (2011) Comparative study of microwave and conventional methods for the preparation and optical properties of novel MgO-micro and nanostructures. J Alloys Compd 509(41):9809–9815

40. Jubu PR et al (2023) An alternative method for estimating the phase fraction of multiphase nanomaterials: analysis from X-ray diffraction. J Appl Sci Nanotechnol 3(3):1–9

41. Xiong G, Pal U, Serrano J, Ucer K, Williams R (2006) Photoluminesence and FTIR study of ZnO nanoparticles: the impurity and defect perspective. Phys Status Solidi C 3(10):3577–3581

42. Al-kifaie AMA (2020) FTIR-Spectrum of Zinc nanoparticle by Laser ablation technique in liquid. In IOP Conf Ser Mater Sci Eng 928(7):072050: IOP Publishing

43. Samy A, El-Sherbiny AE, Menazea A (2019) Green synthesis of high impact zinc oxide nanoparticles. Egyptian Journal of Chemistry, 62, no. The First International Conference on Molecular Modeling and Spectroscopy 19–22 February, 2019, pp 29–37

44. Karthik K, Jaya NV, Kanagaraj M, Arumugam S (2011) Temperature-dependent magnetic anomalies of CuO nanoparticles. Solid State Commun 151(7):564–568

45. Sudha V, Murugadoss G, Thangamuthu R (2021) Structural and morphological tuning of Cu-based metal oxide nanoparticles by a facile chemical method and highly electrochemical sensing of sulphite. Sci Rep 11(1):3413

46. El-Trass A, ElShamy H, Mehasseb I, El-Kemary M (2012) CuO nanoparticles: synthesis, characterization, optical properties and interaction with amino acids. Appl Surf Sci 258:2997–3001

47. Swarnkar R, Singh S, Gopal R (2011) Effect of aging on copper nanoparticles synthesized by pulsed laser ablation in water: structural and optical characterizations. Bull Mater Sci 34:1363–1369

48. Yousefi S, Ghasemi B (2020) Precipitator concentration-dependent opto-structural properties of MgO nanoparticles fabricated using natural brine. SN Appl Sci 2:1–10

49. Dar M, Varshney D (2018) Structures and properties of Mg 0.95 Mn 0.01 TM 0.04 O (TM= Co, Ni, and Cu) nanoparticles synthesized by sol–gel auto combustion technique. RSC Adv 8(25):14120–14128

50. Lillo-Ramiro J et al (2021) Optical and microstructural characteristics of CuO thin films by sol gel process and introducing in non-enzymatic glucose biosensor applications. Optik 229:166238

51. Varughese G, Rini V, Suraj S, Usha K (2014) Characterisation and optical studies of copper oxide nanostructures doped with lanthanum ions. Adv Mater Sci 14(4):49–60

52. Arun K, Batra A, Krishna A, Bhat K, Aggarwal M, Francis PJJ (2015) Surfactant free hydrothermal synthesis of copper oxide nanoparticles. Am J Mater Sci 5(3A):36–38

53. Sankar R et al (2014) Green synthesis of colloidal copper oxide nanoparticles using Carica papaya and its application in photocatalytic dye degradation. Spectrochim Acta A Mol Biomol Spectrosc 121:746–750

54. Hajipour MJ et al (2012) Antibacterial properties of nanoparticles. Trends Biotechnol 30(10):499–511

55. Tiwari M, Narayanan K, Thakar MB, Jagani HV, Venkata Rao J (2014) Biosynthesis and wound healing activity of copper nanoparticles. IET Nanobiotechnol 8(4):230–237